4. Y. Sugimoto *et al.*, *Nat. Mater.* **4**, 156 (2005).
5. Y. Sugimoto *et al.*, *Science* **322**, 413 (2008).
6. M. Ternes, C. P. Lutz, C. F. Hirjibehedin, F. J. Giessibl, A. J. Heinrich, *Science* **319**, 1066 (2008).
7. M. Ashino, A. Schwarz, T. Behnke, R. Wiesendanger, *Phys. Rev. Lett.* **93**, 136101 (2004).
8. M. Ashino *et al.*, *Nat. Nanotechnol.* **3**, 337 (2008).
9. Ch. Loppacher *et al.*, *Phys. Rev. Lett.* **90**, 066107 (2003).
10. J. Lagoute, K. Kanisawa, S. Fölsch, *Phys. Rev. B* **70**, 245415 (2004).
11. J. Repp, G. Meyer, S. M. Stojkovic, A. Gourdon, C. Joachim, *Phys. Rev. Lett.* **94**, 026803 (2005).
12. J. Repp, G. Meyer, S. Paavilainen, F. E. Olsson, M. Persson, *Science* **312**, 1196 (2006).
13. F. J. Giessibl, *Rev. Mod. Phys.* **75**, 949 (2003).
14. F. J. Giessibl, *Appl. Phys. Lett.* **76**, 1470 (2000).
15. Mainly because of the uncertainty in the spring constant of the cantilever, a systematic error of 30% is estimated for the measured forces.
16. Materials and methods are available as supporting material on *Science* Online.
17. M. Heyde, M. Sterrer, H.-P. Rust, H.-J. Freund, *Appl. Phys. Lett.* **87**, 083104 (2005).
18. L. Bartels *et al.*, *Phys. Rev. Lett.* **80**, 2004 (1998).
19. H. J. Lee, W. Ho, *Science* **286**, 1719 (1999).
20. H. Hölscher, S. M. Langkat, A. Schwarz, R. Wiesendanger, *Appl. Phys. Lett.* **81**, 4428 (2002).
21. B. J. Albers *et al.*, *Nat. Nanotechnol.* **4**, 307 (2009).
22. J. E. Sader, S. P. Jarvis, *Appl. Phys. Lett.* **84**, 1801 (2004).
23. P. Hohenberg, W. Kohn, *Phys. Rev.* **136**, B864 (1964).
24. W. Kohn, L. J. Sham, *Phys. Rev.* **140**, A1133 (1965).
25. CPMD, IBM Corporation and MPI für Festkörperforschung Stuttgart, www.cpmd.org/.
26. J. P. Perdew, K. Burke, M. Ernzerhof, *Phys. Rev. Lett.* **77**, 3865 (1996).
27. D. R. Hamann, *Phys. Rev. B* **40**, 2980 (1989).
28. S. Grimme, *J. Comput. Chem.* **27**, 1787 (2006).
29. The experimental and theoretical distance values z and d could be related to each other, for example, by comparing the position of the force minimum above a certain molecular site. However, the experimental z position of the force minimum varies significantly between measurements with different CO tips (in Fig. 3 the force minimum was already reached at $z \approx 1.2$ Å, whereas in Fig. 4F it is not reached until $z \approx 0.4$ Å). We attribute this to the fact that the tunneling current, and hence the tip height corresponding to the STM set point, strongly depends on the exact adsorption geometry of the CO molecule at the tip apex. Therefore, we abstain from giving an explicit relation between z and d.
30. We thank A. Curioni, J. Repp, and R. Allenspach for valuable discussions and comments and M. Heyde and F. J. Giessibl for fruitful discussions on instrumental issues. The research leading to these results has received funding from the Swiss National Center of Competence in Research (NCCR) "Nanoscale Science" and from the European Community's Seventh Framework Programme under grant agreement no. 214954 (HERODOT). P.L. gratefully acknowledges funding by the Nederlandse Organisatie voor Wetenschappelijk Onderzoek (Chemical Sciences, Vidi-grant 700.56.423).

Supporting Online Material

www.sciencemag.org/cgi/content/full/325/5944/1110/DC1
Materials and Methods
Figs. S1 to S5
References

12 May 2009; accepted 2 July 2009
10.1126/science.1176210

Amplifying the Pacific Climate System Response to a Small 11-Year Solar Cycle Forcing

Gerald A. Meehl,[1]* Julie M. Arblaster,[1,2] Katja Matthes,[3,4] Fabrizio Sassi,[5] Harry van Loon[1,6]

One of the mysteries regarding Earth's climate system response to variations in solar output is how the relatively small fluctuations of the 11-year solar cycle can produce the magnitude of the observed climate signals in the tropical Pacific associated with such solar variability. Two mechanisms, the top-down stratospheric response of ozone to fluctuations of shortwave solar forcing and the bottom-up coupled ocean-atmosphere surface response, are included in versions of three global climate models, with either mechanism acting alone or both acting together. We show that the two mechanisms act together to enhance the climatological off-equatorial tropical precipitation maxima in the Pacific, lower the eastern equatorial Pacific sea surface temperatures during peaks in the 11-year solar cycle, and reduce low-latitude clouds to amplify the solar forcing at the surface.

It has long been noted that the 11-year cycle of solar forcing is associated with various phenomena in Earth's climate system, in both the troposphere and stratosphere (*1*–*9*). Because the amplitude of the solar cycle (solar maximum to solar minimum) is relatively small, about 0.2 W m^{-2} globally averaged (*10*), and the observed global sea surface temperature (SST) response of about 0.1°C would require more than 0.5 W m^{-2} (*11*), there has always been a question regarding how this small solar signal could be amplified to produce a measurable response.

Postulated mechanisms that could amplify the relatively small solar forcing signal to produce such responses in the troposphere include changes in clouds in the troposphere caused by galactic cosmic rays, or associated global atmospheric electric circuit variations, though neither has been plausibly simulated in a climate model. However, there are two other plausible mechanisms, though each has not yet produced a modeled response of the magnitude seen in the observations. The first involves a "top down" response of stratospheric ozone to the ultraviolet (UV) part of the solar spectrum that varies by a few percent. Peaks in solar forcing cause the enhanced UV radiation, which stimulates additional stratospheric ozone production and UV absorption, thus warming that layer differentially with respect to latitude. The anomalous temperature gradients provide a positive feedback through wave motions to amplify the original solar forcing. The changes in the stratosphere modify tropical tropospheric circulation and thus contribute to an enhancement and poleward expansion of the tropical precipitation maxima (*5*, *12*–*16*). The first demonstration of the top-down mechanism in a modeling study showed a broadening of the Hadley cells in response to enhanced UV that increased as the solar-induced ozone change was included (*17*).

A second "bottom up" mechanism that can magnify the response to an initially small solar forcing involves air-sea coupling and interaction with incoming solar radiation at the surface in the relatively cloud-free areas of the subtropics. Thus, peaks in solar forcing produce greater energy input to the ocean surface in these areas, evaporating more moisture, and that moisture is carried by the trade winds to the convergence zones where more precipitation occurs. This intensified precipitation strengthens the Hadley and Walker circulations in the troposphere, with an associated increase in trade wind strength that produces greater equatorial ocean upwelling and lower equatorial SSTs in the eastern Pacific, a signal that was first discovered in observational data (*1*, *2*). The enhanced subsidence produces fewer clouds in the equatorial eastern Pacific and the expanded subtropical regions that allow even more solar radiation to reach the surface to produce a positive feedback (*18*, *19*). Dynamical air-sea coupling produces a transition to higher eastern equatorial SSTs a couple of years later (*20*, *21*). There is observational evidence for a strengthened Hadley circulation in peak solar forcing years associated with intensified tropical precipitation maxima, a stronger descending branch in the subtropics, and a stronger ascending branch in the lower latitudes (*3*); a poleward expansion of the Hadley circulation in peak solar years, with stronger ascending motions at the edge of the rising branch, as well as a stronger Walker circulation with enhanced upward motions in the tropical western Pacific connected to stronger descending motions in the tropical eastern Pacific (*7*); and enhanced summer season off-equatorial climatological monsoon precipitation over India (*6*, *22*). This cold event–like response to peak solar forcing is different from cold events (also known as La Niña events)

[1]National Center for Atmospheric Research, Post Office Box 3000 Boulder, CO 80307, USA. [2]Center for Australian Weather and Climate, Bureau of Meteorology, Melbourne, Australia. [3]Helmholtz Centre Potsdam – GFZ German Research Centre for Geosciences, Potsdam, Germany. [4]Institut für Meteorologie, Freie Universität Berlin, Berlin, Germany. [5]Naval Research Laboratory, Washington, DC 20375, USA. [6]Colorado Research Associates, Boulder, CO 80301, USA.

*To whom correspondence should be addressed. E-mail: meehl@ncar.ucar.edu

in the Southern Oscillation in that, among other things, zonal wind anomalies in the stratosphere are opposite in sign (*23*).

The top-down stratospheric UV ozone mechanism and the bottom-up coupled air-sea response mechanism have been simulated separately in various climate model experiments that seem to produce elements of the observations, with some evidence of enhancement of off-equatorial tropical precipitation maxima, and a poleward expansion of the Hadley circulation (*5*, *12*, *13*, *16*, *19*, *24*, *25*). A critical weakness of these studies is that either alone does not seem to produce the signals of the amplitude seen in the observations, and no model simulation has been able to simultaneously include both mechanisms with time-evolving 11-year solar cycle forcing. Up until now it was speculated that these two mechanisms could be additive and thus amplify the small solar forcing signal to produce responses more comparable in amplitude to those seen in observations (*19*). Here

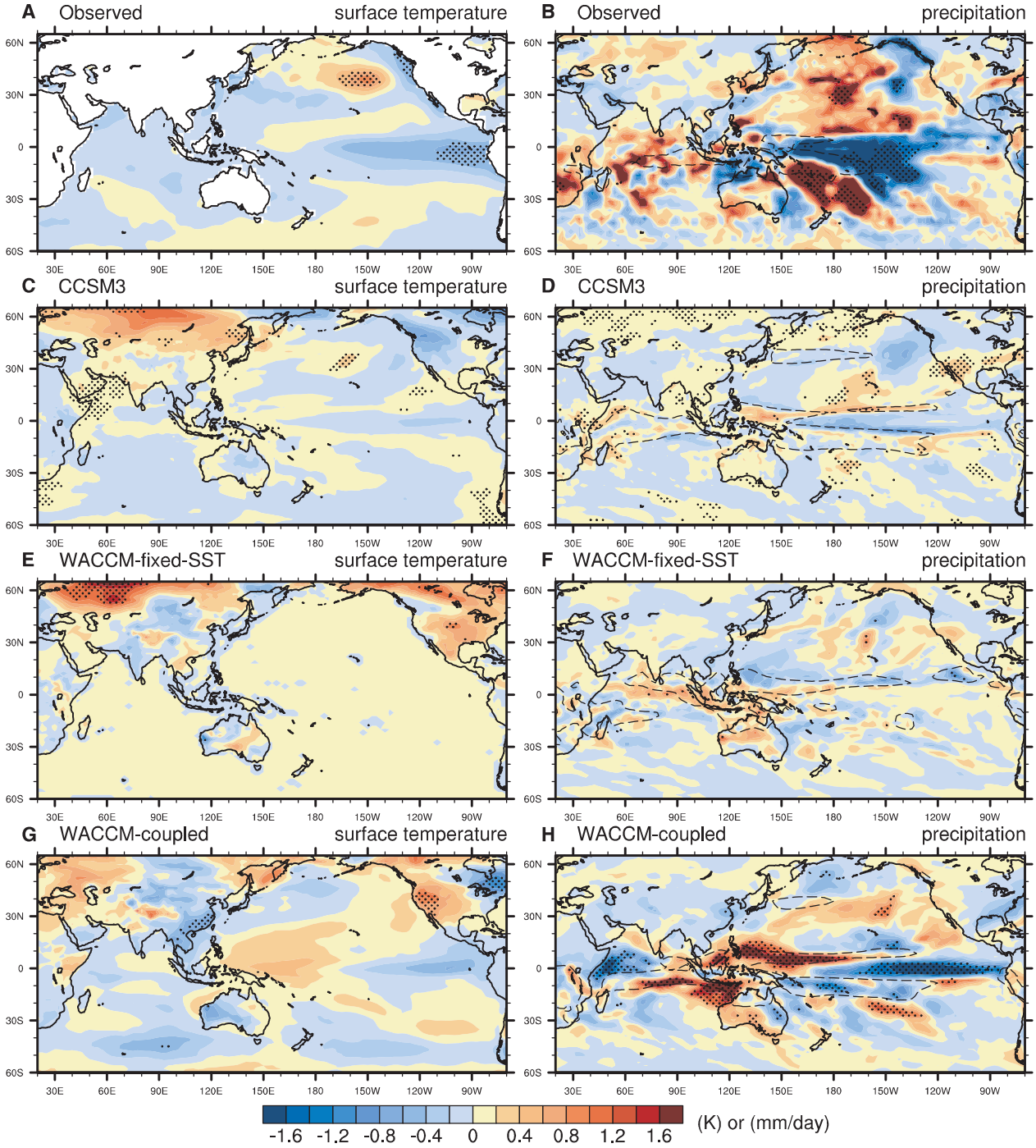

Fig. 1. Composite averages for DJF for peak solar years. (**A**) Observed SSTs for 11 peak solar years (*2*) (°C). (**B**) Same as (A) except for precipitation for three available peak solar years (*2*) (mm day^{-1}). (**C**) Same as (A) except for CCSM3 average of five ensemble members for 20th-century climate (*19*) (°C). (**D**) Same as (C) except for precipitation (*19*) (mm day^{-1}). (**E**) Same as (A) except for WACCM with specified nonvarying SSTs, for 10 peak solar years. (**F**) Same as (E) except for precipitation (mm day^{-1}). (**G**) Same as (A) except for WACCM coupled to the dynamical ocean, land, and sea ice components of CCSM3, for 11 peak solar years (°C). (**H**) Same as (G) except for precipitation (mm day^{-1}). Stippling indicates significance at the 5% level, and dashed lines indicate position of climatological precipitation maxima.

we use several related climate model versions wherein we can include both mechanisms separately (an atmospheric model with no stratospheric dynamics or chemistry coupled to ocean, land, and sea ice; an atmospheric model with stratospheric dynamics and ozone chemistry driven by specified SSTs and sea ice) and then combine them (the atmospheric model with stratospheric dynamics and ozone chemistry coupled to the ocean, land, and sea ice) to test if they can, indeed, amplify the climate system response to solar forcing to produce responses of the magnitude seen in the observations.

Composite observations for peaks in the 11-year solar cycle [how peak years are chosen is described in the supporting online material (SOM); all anomalies are computed for composite peak solar years minus climatology; anomalies for peak solar years minus solar minimum years would be about twice as large] show negative SST anomalies in the eastern equatorial Pacific of about −0.8°C (*2*), and poleward-shifted and intensified climatological precipitation maxima in the Pacific [the Intertropical Convergence Zone (ITCZ) north of the equator and South Pacific Convergence Zone (SPCZ) south of the equator] with anomalies greater than +1 mm day^{-1}, with reduced precipitation (and clouds) over the anomalously low SSTs of about the same magnitude but opposite sign, amounting to changes of ~10% in the ITCZ and SPCZ (Fig. 1, A and B).

The first climate model used here is a global coupled climate model [the Community Climate System Model version 3 (CCSM3); see SOM] that has coupled components of atmosphere, ocean, land, and sea ice. It does not have a resolved stratosphere and no interactive ozone chemistry, so the CCSM3 includes only the bottom-up coupled air-sea mechanism. This model is run for five realizations of 20th-century climate with anthropogenic and natural forcings (including the 11-year solar cycle; see SOM). An ensemble average composite for northern winter [December-January-February (DJF)] of 11 peak solar years shows that this model simulates the coupled air-sea response mechanism at the surface in the tropical Pacific with relatively weak negative SST anomalies in the equatorial eastern Pacific (about −0.2°C or a fourth the size of the observed) and an enhanced and poleward-shifted ITCZ and SPCZ precipitation maxima with anomalies of around +0.3 mm day^{-1} (about a third the size of the observations; Fig. 1, A and B), with negative precipitation anomalies over the anomalously cold water in the eastern equatorial Pacific.

The second climate model, a version of the Whole Atmosphere Community Climate Model (WACCM; see SOM) is a global atmospheric model run with climatological SSTs and changes in solar variability (other external forcings are held constant). It has no dynamical coupled air-sea interaction, but does include a resolved stratosphere, fully interactive ozone chemistry that can respond to the UV part of the solar forcing, and thus should include the top-down stratospheric ozone mechanism. The model is run with 11 11-year solar cycles, and composites are formed for the DJF season for peak solar years. Because the SSTs are specified and are the same every year, there is no SST signal in response to solar forcing by design, but there is an enhancement of the tropical climatological precipitation maxima, with increases of up to 0.4 mm day^{-1} in the tropical eastern Indian and western Pacific, and positive anomalies in the ITCZ and SPCZ (Fig. 1, E and F). These precipitation changes are still about a factor of 3 smaller than observed and are more concentrated in regions where there are largest values of climatological precipitation in the equatorial Indian and western Pacific Ocean regions because there is no dynamical ocean response in the tropical Pacific.

The third climate model uses the atmospheric component (WACCM) from the second model above, but it is coupled to the dynamical ocean, land, and sea ice modules in CCSM3. Therefore, this global coupled climate model should include both the top-down stratospheric ozone mechanism and the bottom-up coupled air-sea interaction mechanism. There are negative SST anomalies in the equatorial eastern Pacific of greater than −0.6°C (Fig. 1G), much closer to the observed values of −0.8°C. These are a factor of 3 greater than the CCSM3 that includes only the bottom-up air-sea coupled mechanism. The precipitation anomalies show an enhanced ITCZ and SPCZ in the tropical Pacific and strengthened precipitation in the tropical Indian Ocean with values greater than +1 mm day^{-1} (Fig. 1H), with reduced precipitation over the anomalously cold water in the eastern equatorial Pacific comparable to the observed anomalies (Fig. 1B). Thus, these models indicate that each mechanism acting alone [the bottom-up surface coupled air-sea mechanism in CCSM (Fig. 1, C and D) and the top-down stratospheric ozone mechanism in WACCM (Fig. 1, E and F)] can produce a weak signature of the observed enhancement of the tropical precipitation maxima, but when both act in concert [in the coupled version of WACCM (Fig. 1, G and H)], the two mechanisms work together to produce climate anomalies much closer to the observed values (Fig. 1, A and B), thus amplifying the relatively small solar forcing to produce significant SST and precipitation anomalies in the tropical Indo-Pacific region. This highlights the importance of stratospheric processes working in conjunction with coupled processes at the surface.

Zonal mean precipitation anomalies averaged around the globe for the observations show the enhanced and poleward-shifted off-equatorial precipitation maxima in the tropics with values of greater than +0.2 mm day^{-1} (on the order of 20%), with reduced precipitation in the equatorial region of more than −0.4 mm day^{-1} (Fig. 2). The CCSM3 with only the bottom-up coupled air-sea interaction mechanism shows a weak enhancement of the off-equatorial zonal mean precipitation maxima of less than 0.1 mm day^{-1}, with reduced near-equatorial precipitation of just more than −0.1 mm day^{-1}, a factor of about 4 less then the observations. The WACCM run with specified SSTs (with only the top-down mechanism) shows more of an enhancement of zonal mean precipitation in the equatorial regions of about +0.15 mm day^{-1}, mainly from the greater climatological precipitation in the tropical western

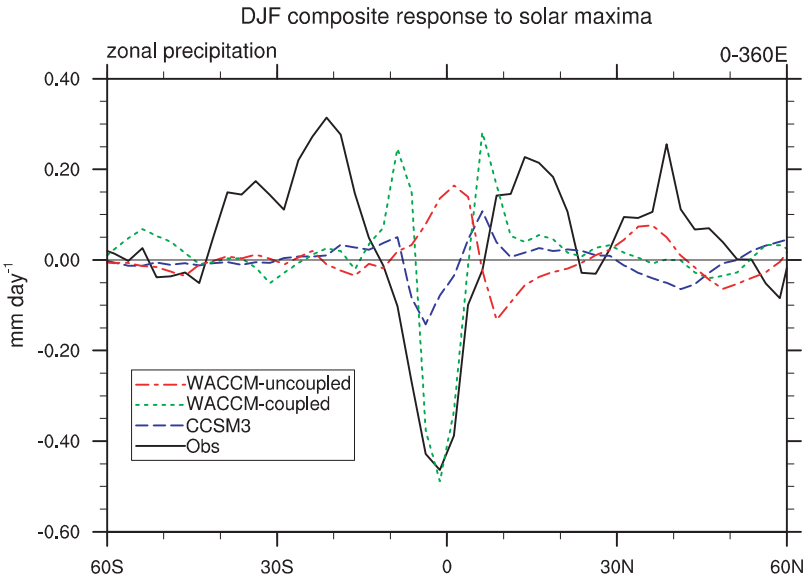

Fig. 2. Global zonal mean precipitation for DJF for 3 peak solar years available in the observations (January–February, black solid line); WACCM uncoupled run with specified SSTs for 11 peak solar years (red dash-dot line); WACCM coupled to the dynamical ocean, land, and sea ice components of CCSM3 for 11 peak solar years (green dashed line); and CCSM3 for five-member ensemble mean of 11 peak solar year composites (blue dashed line). Enhanced off-equatorial tropical precipitation in CCSM3 and WACCM-coupled near 10°N and 10°S are shifted closer to the equator than the observed peaks near 15°N and 20°S because of a systematic error in the coupled models of a too-narrow equatorial Pacific cold tongue.

Pacific and eastern Indian Ocean regions (Fig. 1F). However, the WACCM coupled to the CCSM3 ocean, land, and sea ice components (with both top-down and bottom-up mechanisms) produces an off-equatorial enhancement of zonal mean precipitation more than +0.2 mm day^{-1}, values close to the observed off-equatorial maxima, with a suppression of equatorial zonal mean precipitation that is about the same as the observed values of about −0.45 mm day^{-1}. The coupled WACCM positive zonal mean tropical precipitation anomalies are located closer to the equator compared to the more poleward-shifted observational ones due to the width of the negative SST anomalies in the equatorial Pacific. The observations show negative SST anomalies of amplitude greater than −0.2°C extending from the Date Line to the west coast of South America, and from about 10°N to 10°S (Fig. 1A), whereas the CCSM3 (Fig. 1C) and coupled WACCM (Fig. 1G) have a much narrower latitudinal extent of negative SST anomalies of that magnitude, ranging from only about 5°N to 5°S. This is consistent with a more narrow extent of the climatological eastern Pacific cold tongue that is typical of this class of global coupled climate model (*26*). Therefore, the dynamically coupled interactions in the equatorial eastern Pacific, whereby the trade winds are strengthened in response to the greater upward vertical motions in the intensified precipitation maxima of the ITCZ and SPCZ, produce stronger upwelling of cold water closer to the equator, and thus enhanced ITCZ and SPCZ precipitation maxima closer to the equator in the CCSM3 and coupled WACCM versions compared to the observations (Fig. 2).

The coupled air-sea response mechanism (*18*, *19*) involves locally large net solar flux at the surface compared to the global average, with some values exceeding 1 W m^{-2} locally in the relatively cloud-free areas of the subtropical Pacific in CCSM3 (*19*). The tropical Pacific (30°N to 30°S, 150°E to 90°W) average net solar radiation at the surface of +1.03 W m^{-2} for the coupled WACCM is associated with an overall warming of +0.06°C [the negative areas in the eastern equatorial Pacific are compensated by the positive SST increase in the off-equatorial regions (Fig. 1G)]. This is comparable to the observed global mean surface temperature anomaly of +0.07°C for DJF (*14*) and an estimate of solar maximum to solar minimum variability of observed SSTs for the tropical Pacific area in the year after peak solar forcing of about +0.04°C (fig. S3). However, there is a net solar radiation anomaly at the surface over the tropical Pacific of only +0.1 W m^{-2} for WACCM run with specified nonvarying SSTs, and +0.21 W m^{-2} for CCSM3. To achieve an average warming of the ocean surface layer approaching 0.1°C, there must be a net surface heat flux of more than 0.5 W m^{-2} (*11*, *13*). The globally averaged top-of-atmosphere solar forcing for peak solar years compared to solar minimum years is about 0.2 W m^{-2} (*10*). At the surface at a given location, the diurnal cycle must be taken into account, thus producing about a factor of 2 greater than the global average. All else being equal, there could be about 0.4 W m^{-2} net solar radiation at the surface in regions of the tropics and subtropics for solar maximum to minimum, for an amplitude of 0.2 W m^{-2}. However, for the tropical Pacific, the coupled WACCM version with both solar response mechanisms is producing more than twice that net solar radiation at the surface, with an attendant factor of roughly 4 for surface temperature increase. Despite uncertainties associated with observed surface fluxes derived from reanalysis data (*27*), global tropic-averaged (20°N to 20°S) latent plus sensible heat flux associated with the top-down mechanism could be close to 0.5 W m^{-2} (*28*). The only present model versions that approach that number are coupled WACCM with 0.2 W m^{-2} for the first half of the peak solar year composite for downward latent plus sensible heat flux, and WACCM forced with fixed SSTs with 0.4 W m^{-2} for the first half of the year after peak solar forcing. CCSM3 without the top-down mechanism shows latent plus sensible heat fluxes of near zero for those time periods. However, for coupled WACCM that includes the bottom-up mechanism, the tropic-averaged net solar radiation at the surface for that time period is 0.3 W m^{-2}, roughly three times the amplitude of the solar cycle forcing at the top of the atmosphere, whereas for WACCM forced with fixed SSTs that value is near zero.

This additional amplification of net solar radiation at the surface in coupled WACCM is coming from cloud feedbacks involved with the changes in tropical atmospheric circulation. As the Walker and Hadley cells intensify with their greater vertical motions associated with the enhanced precipitation maxima, there is also greater subsidence in the eastern equatorial Pacific and subtropical Pacific, further reducing cloud amount there and allowing more solar radiation to reach the surface. Both CCSM3 and WACCM run with specified SSTs show some local reductions in cloud amount over regions of the subtropics and eastern equatorial Pacific where there are decreases in precipitation. But in the coupled WACCM, where both mechanisms are active, there is a reduction of tropical Pacific cloud amount of about 2%. Thus, the solar forcing signal is amplified not only by coupled air-sea dynamics and positive ozone-temperature-wind feedbacks, but also by cloud feedbacks in the tropical-subtropical Pacific region. The net effect of these dynamical responses to peaks in solar forcing is that there are negative SST and precipitation anomalies in the tropical Pacific (stronger Walker circulation means stronger trade winds and consequently a coupled dynamical response of greater upwelling of cool water in the equatorial eastern Pacific), and associated cloud feedbacks that provide about a factor of 2 amplification of the net solar forcing at the surface to produce an SST increase of about 0.06°C averaged over the tropical Pacific.

The top-down stratospheric ozone mechanism in the WACCM model versions involves greater absorption of UV solar energy that produces increased ozone in the stratosphere of about 2% with a warming of the stratosphere above 50 hPa [about +0.3° to +0.4°C at 1 hPa averaged over the DJF and March-April-May seasons of the peak solar year for coupled WACCM and WACCM with fixed SSTs, compared to estimates of observed values of +0.8°C in the lower stratosphere (*28*)] that is not present in the CCSM3 without ozone chemistry (shown for December of peak solar years in fig. S1, A, D, and G). These changes in temperature structure in the WACCM model versions produce decreases of westerly-component wind in the lower stratosphere north of about 40°N and increases near 30°N and 30°S (fig. S1, E and H), changes in wave-propagation characteristics (*14*), and changes in vertical velocity. There is enhanced downward motion in the troposphere near 35°N and 35°S, and intensified upward motion in the tropics (fig. S1, F and I) that is stronger and extends farther into the lower stratosphere than in the CCSM3 (fig. S1C).

The nature of the changes in vertical motion in the tropical troposphere relate in part to the coupled response at the surface. WACCM with specified SSTs shows stronger vertical motion near the equator (fig. S1F) with the enhanced precipitation there (Fig. 2). WACCM coupled to the dynamical ocean with negative equatorial Pacific SST anomalies (Fig. 1) has greater vertical motion in the ITCZ and SPCZ with descending motion near the equator (fig. S1I). There is also a poleward shift of the subtropical jet in the troposphere in both WACCM versions that is strongest with the dynamical ocean coupling (positive zonal wind anomalies near 40°N and 40°S and negative anomalies near 20°N and 20°S in the upper troposphere near 200 hPa; fig. S1, E and H). The evolution to the following June also shows the strongest response in the WACCM coupled to the dynamical ocean, with warming in the troposphere of around +0.2°C (fig. S2G) that is comparable to an observational estimate of about the same amount (*28*). This goes along with the transition to higher equatorial Pacific SSTs following peak solar years (fig. S3), intensified upward vertical motion near 10° to 20°N (fig. S2K) associated with stronger monsoon precipitation as seen in observations [e.g., (*1*, *6*)], and anomalous descent near 5°S. Further discussion of the temperature response due to solar forcing is given in the SOM.

An extensive set of model simulations that included a nondynamic mixed-layer ocean (*25*) produced similar responses to the present coupled WACCM experiments [maximum ozone increase of about 2% near 10 hPa, stratospheric warming with an amplitude of about 0.3°C (or 0.6°C solar maximum minus minimum), climatological off-equatorial precipitation enhancement, and an expansion of the Hadley circulation]. However, the inclusion of a dynamical ocean component in the present experiments simulates the cold event–like response and associated cloud feedbacks at peaks of solar forcing due to coupled atmosphere-ocean dynamics that the nondynamic ocean could not produce (*25*).

The role of the Quasi-biennial Oscillation (QBO) in the response to solar forcing has been noted in earlier studies (*3*). A set of experiments with the two WACCM model versions with a prescribed QBO has been carried out, and results from those experiments will be presented in a subsequent paper. However, the results for the climate system response to solar forcing are qualitatively similar to those presented here without the QBO, but the prescribed QBO shows improvements in the stratospheric response compared to observations. Though the solar-forced eastern equatorial SST anomalies shown here are about half the amplitude of those associated with the El Niño–Southern Oscillation, they are relevant for understanding decadal timescale variability in the Pacific. This response also cannot be used to explain recent global warming because the 11-year solar cycle has not shown a measurable trend over the past 30 years (*10*).

References and Notes

1. H. van Loon, G. A. Meehl, J. M. Arblaster, *J. Atmos. Sol. Terr. Phys.* **66**, 1767 (2004).
2. H. van Loon, G. A. Meehl, D. J. Shea, *J. Geophys. Res.* **112**, D02108 (2007).
3. H. van Loon, K. Labitzke, *Meteorol. Z. (Berlin)* **3**, 259 (1994).
4. J. Lean, D. Rind, *Science* **292**, 234 (2001).
5. J. Haigh, M. Blackburn, R. Day, *J. Clim.* **18**, 3672 (2005).
6. K. Kodera, *Geophys. Res. Lett.* **31**, L24209 (2004).
7. H. Gleisner, P. Thejll, *Geophys. Res. Lett.* **30**, 1711 (2003).
8. W. B. White, J. Lean, D. R. Cayan, M. D. Dettinger, *J. Geophys. Res.* **102**, 3255 (1997).
9. D. Rind, *Science* **296**, 673 (2002).
10. J. Lean, G. Rottman, J. Harder, G. Kopp, *Sol. Phys.* **230**, 27 (2005).
11. W. B. White, D. R. Cayan, J. Lean, *J. Geophys. Res.* **103**, 21,355 (1998).
12. N. Balachandran, D. Rind, P. Lonergan, D. Shindell, *J. Geophys. Res.* **104**, 27,321 (1999).
13. D. Shindell, D. Rind, N. Balachandran, J. Lean, J. Lonergan, *Science* **284**, 305 (1999).
14. K. Kodera, Y. Kuroda, *J. Geophys. Res.* **107**, 4749 (2002).
15. J. Haigh, *Philos. Trans. R. Soc. London A* **361**, 95 (2003).
16. K. Matthes, Y. Kuroda, K. Lodera, U. Langematz, *J. Geophys. Res.* **111**, D06108 (2006).
17. J. D. Haigh, *Science* **272**, 981 (1996).
18. G. A. Meehl, W. M. Washington, T. M. L. Wigley, J. M. Arblaster, A. Dai, *J. Clim.* **16**, 426 (2003).
19. G. A. Meehl, J. M. Arblaster, G. Branstator, H. Van Loon, *J. Clim.* **21**, 2883 (2008).
20. G. A. Meehl, J. M. Arblaster, *J. Clim.* **22**, 3647 (2009).
21. W. B. White, W. B. Z. Liu, *Geophys. Res. Lett.* **35**, L19607 (2008).
22. K. Kodera, K. Shibata, *Geophys. Res. Lett.* **33**, L19704 (2006).
23. H. van Loon, G. A. Meehl, *J. Atmos. Sol. Terr. Phys.* **70**, 1046 (2008).
24. D. T. Shindell *et al.*, *Geophys. Res. Lett.* **33**, L24706 (2006).
25. D. Rind, J. Lean, J. Lerner, P. Lonergan, A. Leboissitier, *J. Geophys. Res.* **113**, D24103 (2008)
26. G. A. Meehl, H. Teng, G. W. Branstator, *Clim. Dyn.* **26**, 549 (2006).
27. K. E. Trenberth, J. M. Caron, D. P. Stepaniak, *Clim. Dyn.* **17**, 259 (2001).
28. W. B. White, *J. Geophys. Res.* **111**, C09020 (2006).

29. Portions of this study were supported by the Office of Science (BER), U.S. Department of Energy, Cooperative Agreement No. DE-FC02-97ER62402, and the NSF. The National Center for Atmospheric Research is sponsored by the NSF.

Supporting Online Material

www.sciencemag.org/cgi/content/full/325/5944/1114/DC1
Methods
Figs. S1 to S3
References

27 February 2009; accepted 17 July 2009
10.1126/science.1172872

Good Genes and Good Luck: Ammonoid Diversity and the End-Permian Mass Extinction

Arnaud Brayard,[1]* Gilles Escarguel,[2]* Hugo Bucher,[3,4] Claude Monnet,[3] Thomas Brühwiler,[3] Nicolas Goudemand,[3] Thomas Galfetti,[3] Jean Guex[5]

The end-Permian mass extinction removed more than 80% of marine genera. Ammonoid cephalopods were among the organisms most affected by this crisis. The analysis of a global diversity data set of ammonoid genera covering about 106 million years centered on the Permian-Triassic boundary (PTB) shows that Triassic ammonoids actually reached levels of diversity higher than in the Permian less than 2 million years after the PTB. The data favor a hierarchical rather than logistic model of diversification coupled with a niche incumbency hypothesis. This explosive and nondelayed diversification contrasts with the slow and delayed character of the Triassic biotic recovery as currently illustrated for other, mainly benthic groups such as bivalves and gastropods.

During the Paleozoic and Mesozoic, ammonoids represented an abundant, highly diversified, and geographically widespread group of marine cephalopods. As a major component of open marine biotas, the diversity and evolution of these shelly mollusks closely record the succession of Paleozoic to Mesozoic global changes (*1*–*3*). The Permian is characterized by four major, slowly evolving clades of ammonoids showing a protracted, two-step decline during the Late Permian (Capitanian and Changhsingian extinctions) (*4*). Only three known ammonoid genera among Ceratitida survived the Permian-Triassic boundary (PTB); with very few exceptions, Triassic ammonoids are usually found to root into a single genus and are therefore interpreted as a monophyletic clade (*1*, *3*, *5*, *6*). Their extinction selectivity and patterns of recovery have been addressed through changes of morphological diversity (*7*–*9*), taxonomic richness, endemism, and biogeographical distribution viewpoints (*1*, *2*). One problem has been a lack of absolute age calibration of evolutionary trends across the PTB. We have used diversity analyses combined with recently published radiometric ages (*10*) to show that Triassic ammonoids diversified explosively in the first million years after the PTB.

It has usually been assumed that the end-Permian mass extinction affected ecological assemblages so deeply that the postcrisis biotic recovery spanned the entire Early Triassic [~5 million years (My) (*11*)], if not more (*12*–*14*). To test this scenario, we constructed a global taxonomic data set at the generic level, from the Late Carboniferous [Kasimovian, 307 million years ago (Ma)] to the Late Triassic (Rhaetian, 201.5 Ma). For each time bin, we considered all documented occurrences of ammonoid genera for each major oceanic sedimentary basin. The resulting data table records the occurrence of 860 genera within 77 basins through 25 successive time bins of unequal duration. Paleozoic ammonoid data are independently derived from the last versions of the Goniat and Ammon databases (*15*, *16*); Triassic ammonoid data are compiled from various sources (*10*), with the latest published genera and occurrences added in all cases. Due to distinct taxonomic treatments between the two Paleozoic databases, higher generic richness counts per time bin are obtained from Ammon (Fig. 1), but these differences have no consequence on origination and extinction rate estimates (fig. S1). We thus selected the published Goniat database for further analyses.

For each time bin, we derived the total (observed + inferred; S_{obs}) number of genera and estimated overall generic richness using Chao2 and Jackknife2 nonparametric indices (*10*) (Fig. 1 and table S1). Due to the nature of the available data (generic occurrences within basins), the close correspondence between S_{obs} and Chao2 and Jackknife2 estimators is strong evidence that most time bins have qualitatively similar structures of observed basin incidences resulting from comparable taxonomical practices and sampling efforts along the analyzed time series. There is no evidence that Triassic time bins contain more genera falsely identified as singletons (i.e., genera spanning only one time bin) than Permian ones. When combined with the

[1]UMR-CNRS 5561 Biogéosciences, Université de Bourgogne, 6 Boulevard Gabriel, F-21000, Dijon, France. [2]UMR-CNRS 5125 PEPS, Université Lyon 1, Campus de la Doua, Bât. Géode, 2 Rue Dubois, F-69622 Villeurbanne Cedex, France. [3]Paläontologisches Institut und Museum, Universität Zürich, Karl-Schmid Strasse 4, CH-8006 Zürich, Switzerland. [4]Department of Earth Sciences, ETH Zürich, Switzerland. [5]Department of Geology and Paleontology, University of Lausanne, l'Anthropole, Lausanne, Switzerland.

*To whom correspondence should be addressed. E-mail: arnaud.brayard@u-bourgogne.fr (A.B.); gilles.escarguel@univ-lyon1.fr (G.E.)